



Thermal infrared shadow-hiding in GOES-R ABI imagery: snow and forest temperature observations from the SnowEx 2020 Grand Mesa field campaign

Steven J. Pestana¹, C. Chris Chickadel^{1,2}, Jessica D. Lundquist¹

5 ¹Civil and Environmental Engineering, University of Washington, Seattle 98105, USA

²Applied Physics Laboratory, University of Washington, Seattle 98105, WA, USA

Correspondence to: Steven J. Pestana (spestana@uw.edu)

Abstract. The high temporal resolution of thermal infrared imagery from the geostationary GOES-R satellites presents an opportunity to observe mountain snow and forest temperatures over the full diurnal cycle. However, the off-nadir views of these imagers may impact or bias surface temperature observations, especially when viewing a surface composed of both snow and forests. We used GOES-16 and -17 thermal infrared brightness temperature observations of a flat snow and forest-covered study site at Grand Mesa, Colorado, USA, to characterize how forest coverage and view angle impact these observations. These two geostationary satellites provided views of the study area from the southeast (134.1° azimuth, 33.5° elevation) and southwest (221.2° azimuth, 35.9° elevation) respectively. Coincident ground-based and airborne IR observations collected as part of the NASA SnowEx field campaign in February 2020 provided a rich dataset for comparison. Observations over the course of two cloud-free days spanned the entire study site. The surface temperature observations from each dataset were compared to find their relative differences, and how those differences may have varied over time or as a function of varying forest cover across the study area. GOES-16 and -17 surface brightness temperatures were found to match the diurnal cycle and temperature range within ~1 hour and ± 3 °C of ground-based observations. GOES-16 and -17 were both biased warmer than nadir-looking airborne IR and ASTER observations. The warm biases were higher at times when the sun-satellite phase angle was near its daily minimum, and the warm biases seen in GOES-16 were greater for pixels that contained more forest coverage. The observations suggest that a “thermal infrared shadow-hiding” effect may be occurring, where the geostationary satellites are preferentially seeing the warmer sunlit sides of trees at different times of day. These biases are important to understand for applications using GOES-R ABI for surface temperatures over areas with surface roughness features, such as forests, that could exhibit a thermal infrared shadow-hiding effect.

1 Introduction

Mountain areas that receive seasonal snow are the headwaters of rivers that more than a billion people depend on globally (Immerzeel et al., 2020). Despite their importance, these are notoriously difficult places to gather hydrological or



30 meteorological observations for predicting snow water equivalent (SWE) and the timing and magnitude of streamflow
(Raleigh et al., 2013). Longwave radiation measurements, of which the upwards component is controlled by the diurnal
cycle of snow surface temperature, has been identified as especially critical for modeling these snowmelt fed systems (Lapo
et al., 2015; Raleigh et al., 2016). Distributed observations of surface temperatures at sub-daily temporal resolutions are
needed for hydrologic and land surface models, and could aid real-time forecasting (Shamir and Georgakakos, 2014).
35 Thermal infrared (TIR) imagery from geostationary satellites that constantly view the same portions of Earth's surface, such
as GOES-R ABI, can make land surface temperature observations at very high temporal resolution (5 minutes or better),
capturing the full diurnal cycle. These observations, however, have spatial resolutions of 2+ km, and view the land surface
from off-nadir angles.

The 2020 NASA SnowEx field campaign was a collaborative effort between government agencies and academic researchers
40 to intercompare and evaluate snow remote sensing methods with extensive ground based observations. This was conducted
in early 2020 at Grand Mesa, a large flat-topped mountain in the western part of the US state of Colorado. As part of this
campaign, a multi-sensor experiment was designed to investigate how the off-nadir views of GOES-R satellites affect their
surface temperature retrievals over snow and forests by making surface temperature observations and intercomparisons at a
range of spatial and temporal scales (Table 1, Figure 1). This unique study site, a flat expanse of snow and conifer forest,
45 allowed us to investigate how forests affect surface temperature observations, independent of the effects due to complex
terrain. Ground based snow surface temperature measurements provided a continuous point of comparison for GOES-R,
while multiple overpasses from airborne IR imagery, gridded to 5 m spatial resolution, provided finer resolution distributed
surface temperature details over the course of two mornings. To benchmark the ground point measurements and airborne IR,
which itself has a wide range of view angles (Pestana et al., 2019), we compared these with a coincident nadir-looking
50 ASTER TIR image at 90 m spatial resolution. Specifically, we set out to address the following questions regarding GOES-R
ABI surface temperature observations during SnowEx: 1) What were the relative accuracies of each source of remotely
sensed surface temperature? 2) How did fractional forest cover impact the relative accuracy of GOES-R ABI surface
temperature across the study area? 3) How did the relative accuracy of GOES-R ABI surface temperature change over the
course of each day of observations?

55 We hypothesized that among the surface temperature observations collected, the best agreements would be between the
nadir-looking ASTER, nadir-looking Airborne IR, and ground based snow surface temperatures. We further hypothesized
that for GOES-R ABI pixels with greater forest canopy, the observed surface brightness temperatures would be greater than
those from the nadir ASTER and Airborne IR imagery. Finally, we hypothesized that these warm biases would be greatest in
the early morning observations by GOES-16 (East) and late afternoon observations by GOES-17 (West), when they are
60 viewing the solar-illuminated side of trees.

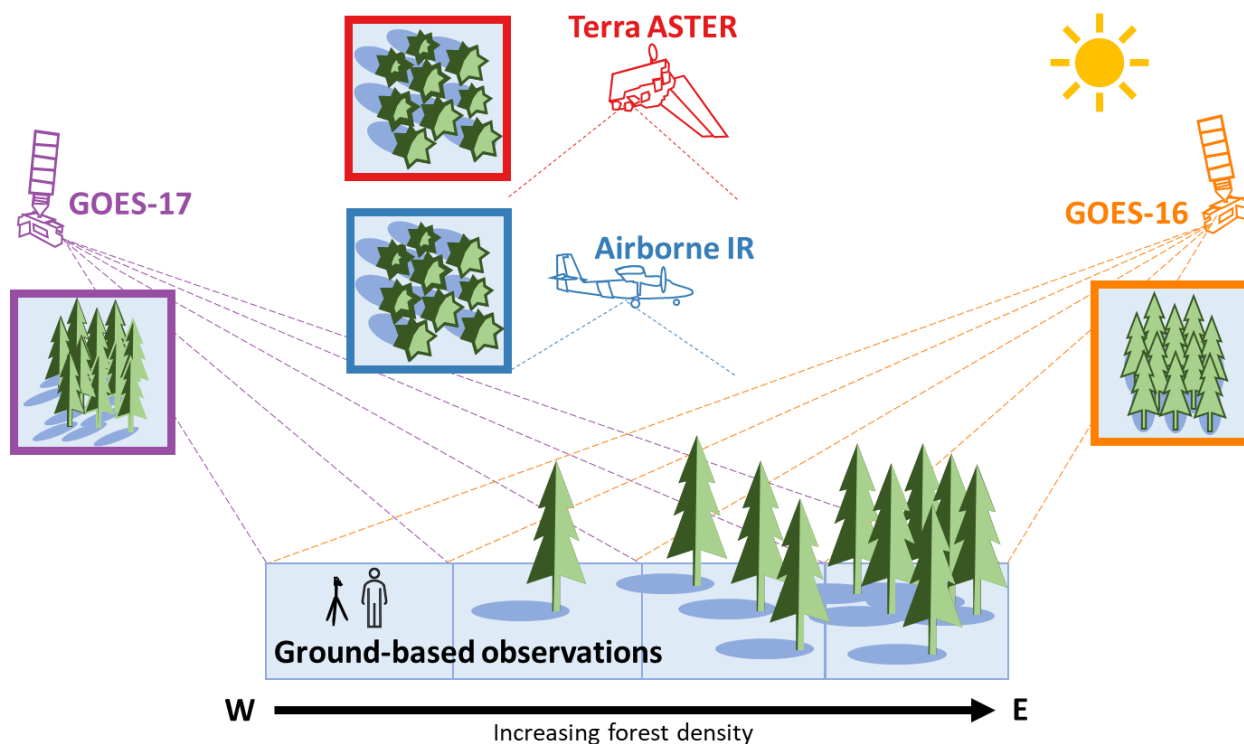


Figure 1. Conceptual illustration of how nadir and off-nadir looking remote sensing imagers see parts of a forest canopy and, depending on the direction of solar illumination, the shadows cast by trees.

1.1 High temporal resolution TIR imagery

65 Land surface models are highly sensitive to their temperature and longwave forcing input (Mizukami et al., 2014; Raleigh et al., 2015; Islam & Dery, 2016), in both accumulation and ablation periods (Gunther et al., 2019). This is especially important for sparsely instrumented mountain areas, where land surface models can have air temperature errors of ~3-4 °C (Tomasi et al., 2017). Differences in forcing inputs, or how surface energy fluxes are parameterized in land surface models, can result in hourly surface temperature errors as much as of 15 °C (Essery et al., 2013), and lead to snow disappearance date

70 uncertainties spanning months (Hinkelman et al., 2015). Surface temperature observations at model-relevant time steps, such as hourly temporal resolutions, are needed especially to capture diurnal processes like snow melt-freeze cycles (Niu et al., 2011) and snow grain metamorphism, which in turn drive feedbacks in the surface energy balance through changes in emissivity and albedo (Flanner and Zender, 2006; Warren, 1982, 2019).

Thermal infrared (TIR) satellite imagery can provide snow surface temperature observations for homogenous snow-covered

75 landscapes (Hall et al., 2008; Wan et al., 2002), estimates of near-surface air temperature (Pepin et al., 2016; Shamir & Georgakakos, 2014), and dewpoint temperature (Raleigh et al., 2013), all of which are needed for modeling hydrologic processes. However, satellite observations at <100 m spatial resolution are made too infrequently (4-16 day repeat) for



looking at snow surface energy balance processes at model-relevant timesteps. Observations from imagers like VIIRS or MODIS (250 m to 1 km resolution) provide two observations per day each for mid-latitude locations. The observations from the sun-synchronous orbiting MODIS or VIIRS imagers do not necessarily see the coldest and warmest times of day to capture the full diurnal temperature range (DTR), nor do they provide land surface temperature (LST) more frequently than every several hours. Their twice daily observations can also be obscured by cloud cover, creating large data gaps relative to the diurnal cycle of snow surface temperatures.

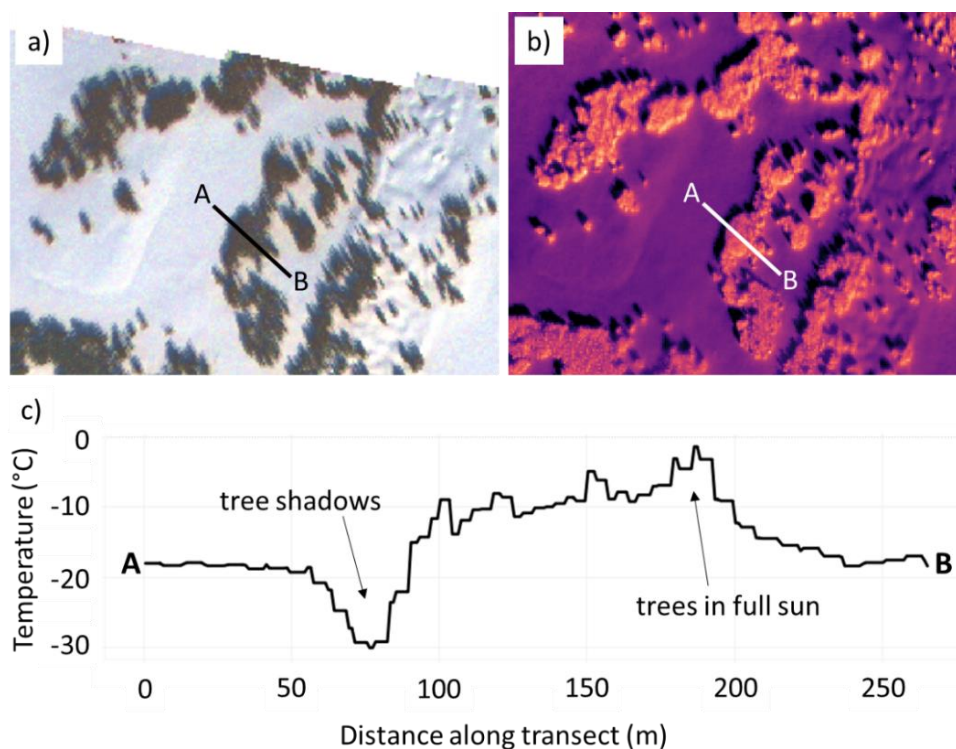
Geostationary satellite imagery may help overcome these drawbacks, providing high temporal resolution surface temperature observations, potentially seeing between intermittent periods of cloud cover, though at coarser spatial resolutions (2+ km) and off-nadir view angles. In the complex terrain and forest vegetation of mountain watersheds, the individual image pixels from TIR observations will report a land surface temperature signature that is a mixture of the subpixel snow and forest surface temperatures (Dozier, 1981; Selkowitz et al., 2014). Snow and vegetation can have significant temperature differences, especially on clear days where incoming solar radiation warms forest canopies more than the high albedo snow surface and during the snowmelt period, when daytime snow surface temperatures are capped at 0 °C (Pestana et al., 2019).

1.2 Off-nadir views and shadow-hiding

Imagery from geostationary satellites comes with the drawback of having off-nadir view angles, dependent on where the area of interest is located relative to the satellite's orbital position (Schmit et al., 2017). GOES-R views the mountains of North America from the south, and in the daytime, south-facing slopes receiving solar illumination heat up more than shaded north-facing slopes. Certain steep north-facing mountain slopes may be completely occluded from view. Prior work compared off-nadir GOES-16 TIR imagery to coincident nadir-looking ASTER and MODIS TIR imagery over the Sierra Nevada of California (Pestana and Lundquist, 2022). This work showed that GOES-16 imagery reported warmer brightness temperatures than ASTER and MODIS, which could see both the sunlit and shaded sides of mountain slopes.

At much smaller spatial scales, similar effects can occur with off-nadir daytime TIR observations of scenes containing forests. Solar illumination, especially at low sun angles, will warm up one side of individual trees or clusters of trees more than the other shaded side. These trees will also cast shadows onto the underlying snow surface, and the snow surface temperature in these shadows can be much colder than snow in sunlight (Figure 2). Therefore, depending on solar illumination and a satellite's view angle, the scene can either appear warmer (solar illuminated, shadows hidden) or colder (shaded areas in view) in comparison to nadir-looking imagery which sees both sides. Shadow-hiding occurs when the imager is viewing from the same direction that the sun is illuminating the scene, such that shadows cast by features such as trees are completely hidden from view (Bréon et al., 2002). This "hotspot" effect has been observed in visible and near-infrared (NIR) imagery over snow and forests (Hall et al., 1993), and over snow with wind forms such as sastrugi (Warren et al., 1998). Analogous to the hotspot effect seen in reflected solar visible and NIR imagery, off-nadir thermal infrared imagery of snow and forests appears warmer than nadir-looking views. At off-nadir view angles, tree profiles come into view, obscuring the colder snow surface behind and beneath them (Balick et al., 2002; Pestana et al., 2019), and these

patterns have been found to change as a function of the relative geometry between the sun and satellite in different seasons (Henderson et al., 2003). With remote sensing at very high temporal resolutions, we can expect to see this effect change over the course of the day as the sun traverses the sky, as different portions of the tree canopy are warmed in direct sunlight, and as tree shadows are cast onto the snow in different directions, creating cooler spots, sometimes hidden from the satellite's
115 view.



120 **Figure 2.** Approximately nadir airborne a) visible and b) IR images over Grand Mesa, Colorado from 2020-02-11 17:25:51 UTC, and c) a temperature profile across a forest stand, showing the presence of very cold tree shadows, and warm southeast forest edges in full sun. The temperature profile is parallel with the view direction of GOES-16, and nearly perpendicular to the view direction of GOES-17.

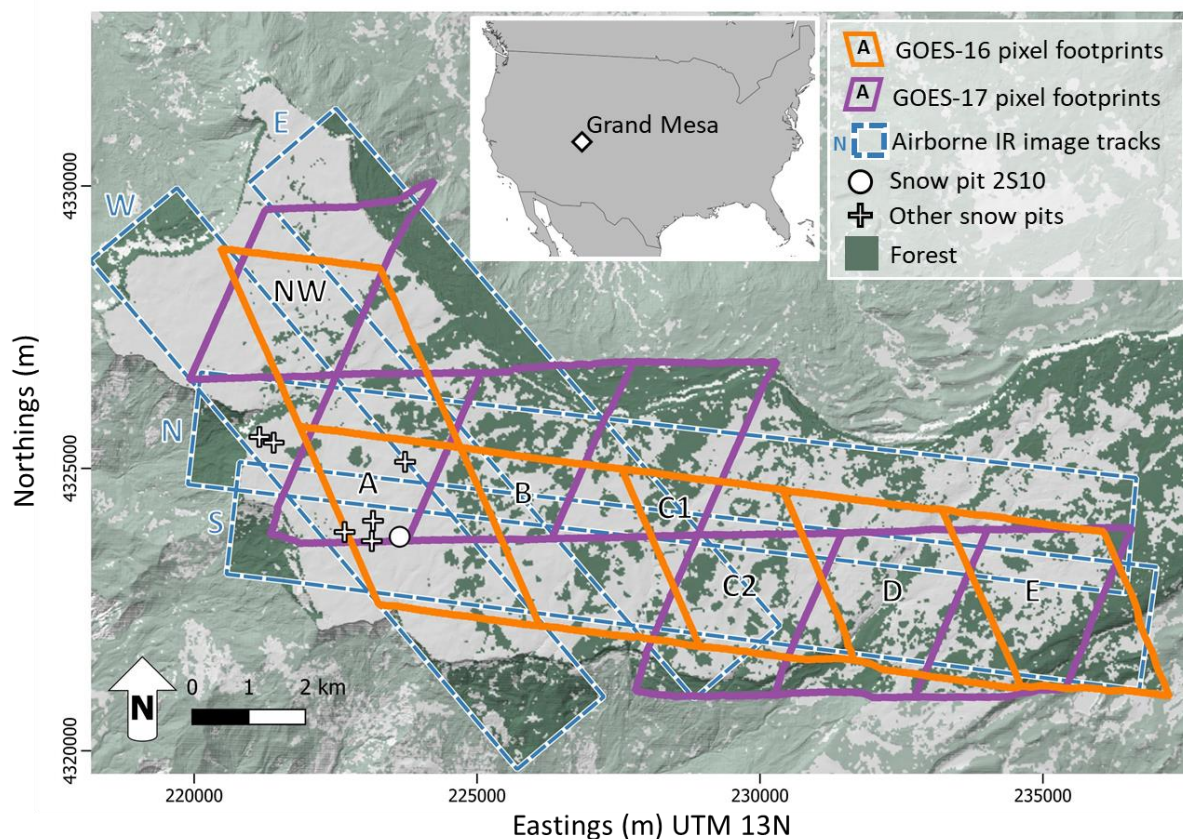
2 Study site and observations

2.1 SnowEx 2020 field campaign study site

The 2020 NASA SnowEx field campaign intensive observation period (IOP) took place at Grand Mesa in western Colorado (39.02°, -108.12°) from 26 January to 14 February 2020 (Figure 3). This period of the field campaign brought together snow
125 remote sensing researchers to test new instruments and methods, and to collect extensive ground-based observations for validation. Grand Mesa, a large flat-topped mountain with elevations above 3000 m, is located within the watersheds of the upper Colorado river and its tributary, the Gunnison River. This region was chosen as a location to evaluate remote sensing



observations of mountain snow because of its flat terrain, where the additional complications of view angles and complex terrain are minimized. The site is also beneficial for thermal infrared remote sensing because at its high elevation, the atmospheric path length, and therefore magnitude of absorption of thermal infrared radiation by water vapor in the atmosphere, is lower than that of sites at lower elevations. The high emissivities of both snow and conifer trees provide us with a scene where surface brightness temperatures are close to true surface temperatures (Kim et al., 2018; Warren, 2019). During the IOP field campaign, the ground surface was entirely snow-covered, with no bare ground surfaces visible in remotely sensed imagery. The westernmost portion of Grand Mesa is sparsely forested, and forest cover increases across the mesa towards the east. Mixed conifer forests of Engelmann spruce (*Picea engelmannii*), subalpine fir (*Abies lasiocarpa*), and lodgepole pine (*Pinus contorta* var. *latifolia*) species dominates the vegetation that stood above the snow, with some stands of deciduous Aspen (*Populus tremuloides*) trees (Currier et al., 2019).



140 **Figure 3. Map of the study area at Grand Mesa, Colorado, and inset map showing its location within the contiguous United States. Polygons outline GOES-16 (orange) and GOES-17 (purple) ABI pixel footprints, and airborne IR image mosaic swaths (blue dashed lines). Snow pit #2S10 where automated continuous snow surface temperatures were observed, is indicated by the white circle, and instantaneous snow surface temperature observations at other snow pits are indicated by white '+'s. Dark green areas indicate forests within the area covered by the thermal infrared remote sensing imagery.**



2.2 Ground-based observations

145 Ground-based observations at Grand Mesa included continuous automated measurements of snow surface temperature, and instantaneous manual snow surface temperatures measurements taken as part of the data collection at individual snow pits. Snow surface temperatures were measured continuously by an Apogee SI-111 radiometer (8 – 14 μm) installed at snow pit #2S10 in the western portion of the mesa (39.0195, -108.19214). This radiometer viewed the snow surface at an angle of 45° from nadir and was mounted 2 m above the ground surface, which at this time was 1.27 m above the snow surface. The radiometer had an instantaneous field of view of 44°, giving it an approximately elliptical footprint of 1.45 m x 2.45 m on the top of the snow surface. Snow surface temperatures measured by this radiometer were recorded at a 5-minute temporal resolution (Pestana and Lundquist, 2021). More than 150 snow pits were dug by the field teams over the course of the IOP (Vuyovich et al., 2021), and among the measurements recorded at each snow pit were snow surface temperature and the time of the surface temperature measurement. Snow surface temperatures were measured by a stem thermometer inserted into the top-most 1 cm of snow and shaded from direct sunlight. These snow pit data were accessed from the SnowEx database through the snowexsql Python library (Johnson et al., 2023). The USGS National Elevation Dataset 1 arc-second (~ 30 m) DEM (US Geologic Survey, 2017) and Tree Canopy Cover (TCC) product from the National Land Cover Database (NLCD) 2016 (Coulston et al., 2012) were used to compute zonal statistics of elevation and fractional vegetated area (f_{veg}), respectively, across the study site.

160 **Table 1. Ground-based and remotely sensed surface temperature observations from the SnowEx 2020 field campaign used in this study.**

	Dataset	Spatial resolution	Temporal resolution	Spectral range	Specified accuracy
Ground-based observations	Continuous snow surface temperature	1.5x2.5 m spot size	5 minute	8 – 14 μm	± 0.2 °C
	Instantaneous snow surface temperature	n/a	n/a	n/a	± 1 °C
Remote sensing observations.	Airborne IR image mosaics	5 m	~10 minute	8 – 14 μm	± 2 °C
	ASTER IR image (AST L1T)	90 m	n/a (one image)	10.95 - 11.65 μm	2%
	GOES-16 and -17 ABI band 13 (ABI-L1b-RadC)	~ 2 km	5 minute	10.05 – 10.55 μm	~ 1.5%
	GOES-16 and -17 ABI band 14 (ABI-L1b-RadC)	~2 km	5 minute	10.8 – 11.6 μm	~ 1.5%
	GOES-16 and -17 ABI LST (ABI-L2-LSTC)	~ 2 km	1 hour	n/a	± 2.5 °C



2.3 Remote sensing observations

2.3.1 GOES-R ABI

165 Images from the Advanced Baseline Imager (ABI) onboard GOES-16 and GOES-17 were retrieved for the duration of the study period in February 2020. The 5-minute temporal resolution Level 1b Radiance CONUS product (L1b-RadC) for thermal infrared bands 13 (10.3 μm) and 14 (11.2 μm), and the 1-hour temporal resolution Level 2 Land Surface Temperature CONUS product (L2-LSTC), were downloaded as NetCDF files via the goespy library (Mello and Pestana, 2022). Both satellites viewed the Grand Mesa study site from similar view angles, though with GOES-16 in the southeastern sky (azimuth 134.1°, or 45.9° from due south) and GOES-17 in the southwestern sky (azimuth 221.2°, or 41.2° from due south), with elevation of angles of 33.5° and 35.9° respectively.

The specific ABI pixel footprints that overlapped the study area on top of Grand Mesa were identified by first orthorectifying (Pestana et al., 2022; Pestana and Lundquist, 2022) 2 km L1b-RadC imagery clipped to the region surrounding Grand Mesa from each of GOES-16 and GOES-17. Vector polygons outlining the ABI pixel footprints were created from these sample images, and the resulting polygons were then used to compute land surface elevation summary statistics from the 30 m resolution DEM (US Geologic Survey, 2017). We sampled ABI pixels with footprints on top of Grand Mesa that covered an area with a mean elevation greater than or equal to 3000 m and standard deviation of elevation less than or equal to 60 m. For GOES-16, this resulted in six pixels selected, and for GOES-17, seven pixels (Figure 3). The pairs of overlapping GOES-16 and -17 pixels were labeled “NW” for the pixels covering the northwestern most portion of Grand Mesa, and “A” – “E” for the pixels running roughly west to east across the study area. Two GOES-17 pixels are labeled “C1” and “C2” to indicate that they both primarily overlapped with GOES-16 pixel “C.” Timeseries of the thermal infrared radiance, brightness temperatures (both from L1b-RadC), and LST (from L2-LSTC) were compiled for each of these pixels from imagery covering 8 to 15 February 2020.

These pixel footprints were used to delineate areas of different fractional vegetation cover for comparison across the mesa. The NLCD TCC map was converted to a binary forest map with a vegetation threshold at 20% TCC. This threshold was chosen to visually match the forest above the snow surface in the ASTER visible image from the morning of 8 February (Figure 6a). For each GOES ABI pixel footprint, the fractional vegetation area (fveg) was calculated as the fraction of the pixel footprint classified as forest in the binary forest map.

Hourly LST observations were not available for most of the daytime periods. The ABI Cloud Mask algorithm is generally used to determine when and where the land surface is not obscured by clouds to determine if LST should be computed. However, identifying cloud cover over snow is notoriously difficult due to their similar appearance in remote sensed imagery across the visible through infrared spectrum (Rittger et al., 2019; Stillinger et al., 2019). Only four daytime LST observations on 8 February were available, and on 11 February there were three daytime and nine nighttime LST observations. Therefore, we focus primarily on radiance and brightness temperature in our analysis.



195 2.3.2 Airborne IR imagery

Airborne IR imagery (Chickadel et al., 2022) was collected on four days with the UW Applied Physics Laboratory's Compact Airborne System for Imaging the Environment (CASIE), consisting of thermal infrared cameras and an infrared radiometer, mounted on the Twin Otter research aircraft from the Naval Postgraduate School (NPS) Center for Interdisciplinary Remotely Piloted Aircraft Studies (CIRPAS). CASIE was installed on the aircraft to be primarily nadir-
200 looking, and had three DRS UC640-17 TIR cameras (8 – 14 μm) pointing with bore-sight incidence angles of 19°, 0° (nadir-looking), and 21° from port to starboard on the aircraft. These three cameras have overlapping fields of view of 25° (left camera) and 40° (center and right cameras) perpendicular to the aircraft flight direction, with a total field of view of about 72.5° (Lundquist et al., 2018). The aircraft flew at about 1 km above the top of Grand Mesa, giving the three cameras a total
205 swath width of about 2.5 km perpendicular to the direction of flight, and a raw ground resolution of 1 m. A nadir-looking Heitronics KT15.85D infrared radiometer with spectral range 9.6-11.5 μm and narrow 1.9° field of view provides a precise brightness temperature measurement for a spot on the ground surface at the center of the center camera's field of view. This higher precision radiometer data was used to calibrate the TIR cameras (Pestana et al., 2019) prior to mosaicking images together using the aircraft INS-GPS navigation data from their original ~1.1 m spatial resolution to 5 m.

Flightlines over the study site were along two sets of parallel tracks that would overlap with ground observations at snow pits
210 (Figure 3). One set of parallel tracks ran east-west, and the other tracks ran roughly northwest-southeast to capture the northwest portion of the mesa. The airborne IR imagery collection was in part planned to coincide with the collection of satellite imagery by ASTER on 8 February.

2.3.3 Terra ASTER

The NASA Terra satellite made an overpass of the Grand Mesa study site and imaged it with ASTER at 18:07 UTC (11:07
215 MST) on 8 February 2020. ASTER provides a reliable source of surface brightness temperature information at 90 m spatial resolution (Abrams, 2000), fine enough to capture the surface temperature variabilities across the Grand Mesa study area and resolve forest stands from open snow. We used the thermal infrared image of Grand Mesa AST L1T product (Meyer et al., 2015) from band 14 (11.3 μm) converted from digital number to brightness temperature.

3 Methods

220 3.1 Evaluating airborne IR image mosaics against ASTER

To first assess the accuracy of the airborne IR imagery, two airborne IR mosaics from 8 February at 18:07 and 18:19 UTC (11:07 and 11:19 MST), running east-west across the mesa, were compared against the coincident ASTER image captured at 18:07 UTC (11:07 MST). The airborne IR mosaics were first resampled to the same spatial resolution of ASTER by taking the mean of the original 5 m spatial resolution images within each 90 m ASTER pixel. The differences between ASTER and



225 each of the two resampled airborne IR mosaics were then computed, producing two difference maps, and the mean and standard deviation of differences were computed for each. Means and standard deviations of differences were also computed for the portions of the difference maps within each of the GOES-16 ABI pixel footprints. The difference maps were inspected qualitatively for patterns in the imagery across the study site to better characterize properties of the airborne IR imagery.

230 **3.2 Comparison of airborne IR, ASTER and ground observations**

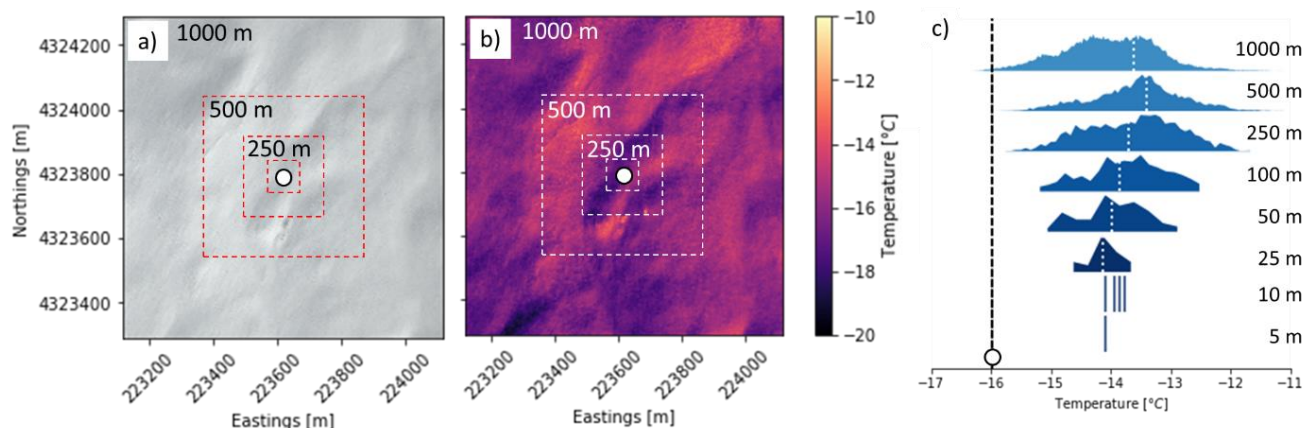
To determine how representative the ground-based point temperature measurements were of their surrounding areas, airborne IR imagery and the single ASTER satellite image were compared with ground-based data at the times when each passed over the study site. From each Airborne IR mosaic, a 1 x 1 km square was extracted from around the automated snow surface temperature measurement site at snow pit #2S10 (Figure 4). Only airborne images that covered at least 30% of this 1
235 km² area were used. The mean, median, and standard deviation of surface temperatures from this area in each airborne IR image were computed. This provided us with a timeseries of snow surface temperatures at each time that the aircraft flew over the ground site. The same 1 km² region around the snow surface temperature measurement site was sampled from the single ASTER image from the morning of 8 February to compute the surface temperature mean, median, and standard deviation as seen by ASTER. The correlation between the timeseries of Airborne IR snow temperature observations and
240 ground-based snow surface temperatures were computed for each day, while the difference between the ground-based snow surface temperature measurements and ASTER observations were computed at the time of its overpass.

To compare the snow surface temperature observations taken at each snow pit against coincident airborne IR imagery, all of the snow pits sampled from 8 February and 11 February that were along the aircraft's flight path within +/- 30 minutes of the flight overpass were compared to the images from that flight. The mean and standard deviation of airborne IR observed
245 surface temperatures within a 100 m² square centered on the snow pit were then compared with these ground-based observations to determine how the differences between the two varied over time and across the study area.

The sensitivity of the comparisons between airborne IR imagery, ASTER, and point ground-based surface temperature observations was tested by reducing the size of the square area from which temperatures were sampled from the airborne IR images (Figure 4), from a square with sides ranging from 1000 m to 100 m (a single ASTER pixel is 90 m), and then for the
250 airborne imagery ranging from 1000 m to 5 m (the size of a single airborne IR pixel) (Table 2). All airborne IR images were included in this analysis, rather than excluding images that covered less than 30% of the area, as was done in the prior analysis of airborne IR and ground data. The mean, median, and standard deviation of surface temperatures were computed for the sampled region in each image. The mean difference, and root mean squared difference between all the airborne IR surface temperature observations of these areas and the coincident ground-based temperature measurements, were computed.
255 The smallest area sampled was a single 5 m airborne IR pixel that should contain the ~2.5 m footprint of the ground-based radiometer that was measuring snow surface temperatures. However, the geolocation accuracy of the airborne IR mosaic



imagery is only about ± 10 m (Pestana et al., 2019). The single-pixel sampled therefore may not actually overlap completely with the ground-based radiometer footprint, but rather be directly adjacent to it.



260 **Figure 4. Airborne a) visible, and b) IR image of the area around the snow surface temperature observation site at snow pit #2S10. Boxes indicate regions from which the mean airborne IR surface temperature information was taken for comparison with the ground-based observations (only the boxes with sides of 1000, 500, 250, and 100 m are shown). Map coordinates are in UTM zone 13N. c) Histograms of the airborne IR surface temperatures from this example image plotted alongside the ground-based snow surface temperature at this time (vertical dashed line).**

265 3.3 Comparison of high temporal resolution GOES-R ABI with continuous ground observations

GOES-16 and -17 brightness temperature observations were compared against the ground-based snow surface temperature observations at snow pit #2S10. A timeseries of brightness temperatures for bands 13 and 14 at 5-minute temporal resolution was created for 8 to 12 February 2020 for the GOES-16 and -17 ABI pixels, which contained snow pit #2S10 (both labeled pixel A). Two cloud-free periods, 8 February (1400 - 0100 UTC), and 11 February (0400 - 0100) were manually identified by inspecting the GOES imagery and brightness temperatures for cold cloud tops obscuring the study site. The ground-based snow surface temperature observations at snow pit #2S10 over these same time periods were resampled to match the 5-minute temporal resolution of GOES ABI brightness temperatures. All timeseries were then smoothed with a 30-minute running mean to remove the highest frequency variability (median $< \pm 0.02$, $\sigma < 0.6$ °C) from the data and fill data gaps. The daily maximum and minimum temperatures and diurnal temperature range (DTR) were then found for both the ground-based snow surface temperature observations, and for the GOES ABI brightness temperatures. The mean and root mean squared difference between GOES ABI brightness temperatures and the ground-based snow and air temperatures were also computed. For 8 February, because there was cloud-cover at night obscuring the study area until 1400 UTC, we only compared the timing of maximum daytime temperature between GOES and the ground-based observations.

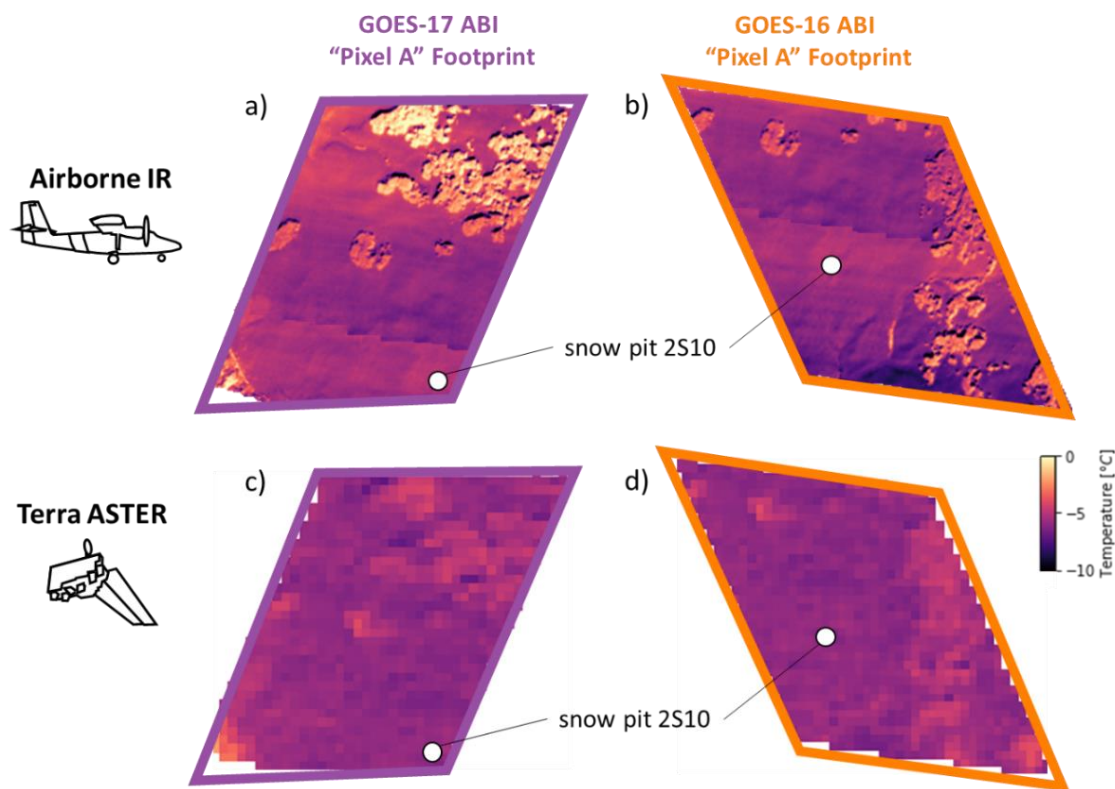
275 3.4 Comparison of GOES-R ABI, airborne IR, and ASTER imagery

280 The differences between GOES-16 and -17 ABI bands 14 and 13 brightness temperatures for 8 February (1400-0000 UTC) and 11 February (0400-0000 UTC) were computed for each pair of corresponding pixels (NW, A, B, C/C1, C/C2, D, and E)



across the mesa. The mean difference, standard deviation of differences, and range of differences for each pixel were plotted against the corresponding pixel's f_{veg} value to inspect for any apparent correlation between these differences and the forest fraction within each pixel footprint. The comparison of GOES-16 to -17 is complicated because they view the scene from different perspectives. For example, the pair of pixels "A" from GOES-16 and -17 overlap each other, but they do not have the same footprint on the ground, have slightly different values of f_{veg} , and may include different amounts of the edges of the mesa.

From each Airborne IR mosaic, if the airborne imagery covered at least 30% of each of the GOES-16 and -17 ABI pixel footprints on top of the mesa, the region was sampled from the mosaic (Figure 5). The mean, median and standard deviation of temperatures within each footprint were computed for comparison against the ABI band 14 brightness temperature and LST of that pixel for a 10-minute window around the aircraft overpass time. Similarly, the GOES-16 and -17 ABI pixel footprints were used to extract surface temperature mean and distributions from the single ASTER image for comparison against ABI band 14 brightness temperatures.



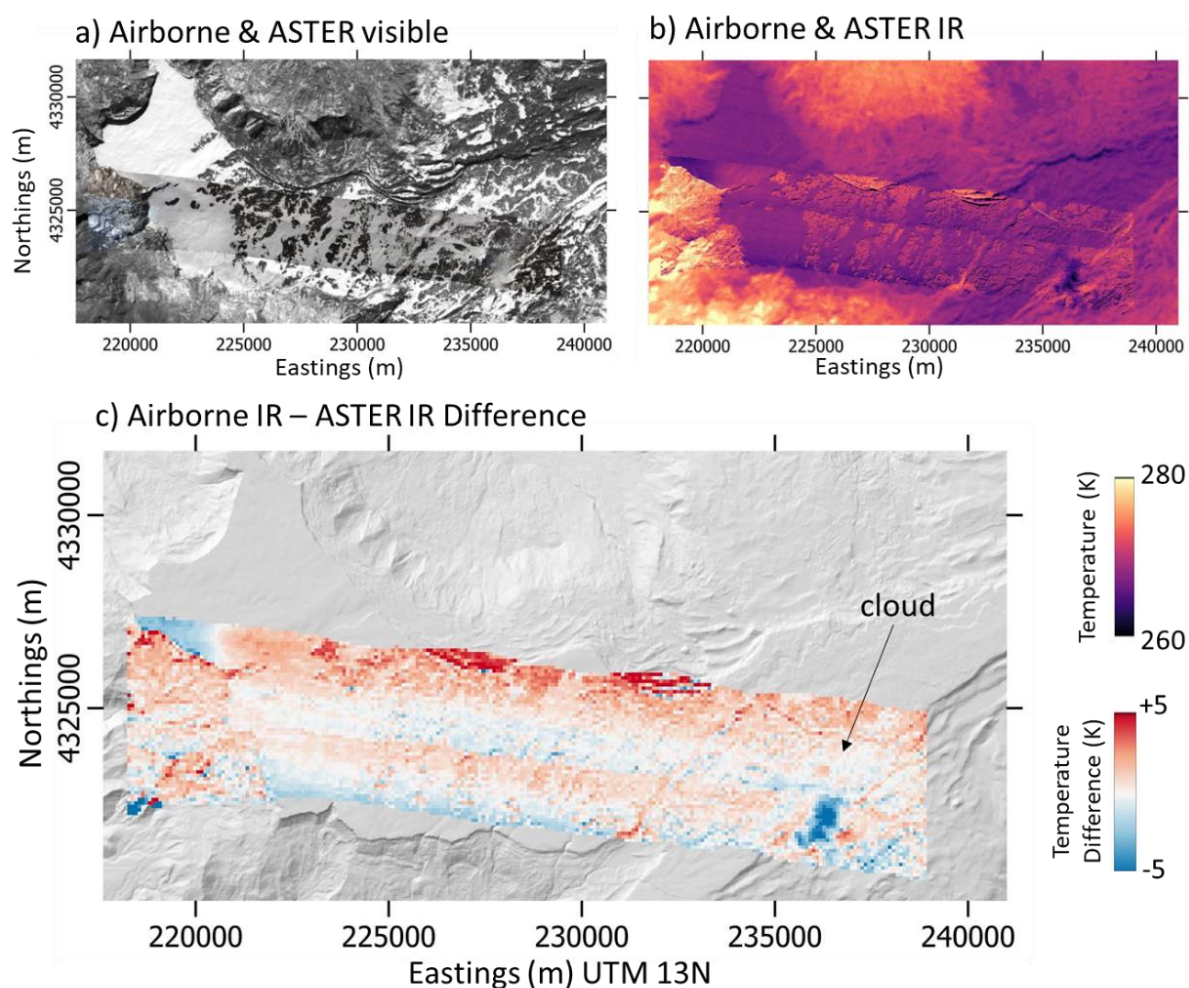
295 **Figure 5. Example of sampling (a,b) 5 m spatial resolution airborne IR image mosaics and (c,d) 90 m spatial resolution ASTER image using the GOES-R ABI pixel footprints.**



4 Results

4.1 Evaluating airborne IR image mosaics against ASTER

The airborne IR imagery was found to have a warm bias compared with ASTER brightness temperatures. The mean differences between the two resampled airborne IR image mosaics and the ASTER image from the morning of 8 February were 0.4 °C and 0.8 °C, and had standard deviations of 1.5 °C and 1.4 °C, respectively. Using the GOES-16 ABI pixel footprints labeled A-E, we found that the mean differences between the airborne IR and ASTER did not vary with vegetation cover.



305 **Figure 6. Comparison of airborne and ASTER a) visible and b) IR observations on the morning of 8 February 2020. c) The difference between airborne IR image mosaics (north flightline at 18:07 and south flightline at 18:19 UTC) and the ASTER image (at 18:07 UTC).**



There were, however, systematic patterns in the difference between airborne IR and ASTER observed surface temperatures (Figure 6). These two airborne IR mosaics exhibited a temperature gradient across the field of view, with the southern edges of each image appearing approximately 1 °C colder than the northern edges, present only in imagery from flying the east-west flightlines. This gradient is most apparent across the relatively uniform open snow of the west side of the mesa. Though centered at nadir, the three airborne IR cameras together have view angles from 31.5° on the left to 41.0° on the right. At larger off-nadir view angles near the image edges more of the sides of trees will be visible (Pestana et al., 2019). On the aircraft's east-west flight across Grand Mesa, the north looking cameras are seeing the south-facing and sunlit side of trees and fewer tree shadows, while south looking cameras are seeing the north-facing side of trees and more snow surface shaded by the trees. This may explain some of the temperature gradient seen in the east-west flight images. Lastly, the easternmost portion of the airborne IR mosaic from 18:19:15 UTC shows a large cold feature, which, by inspecting the visible airborne imagery, we identified as a small cloud, not visible in the airborne or ASTER image from 12 minutes prior.

4.2 Comparison of airborne IR, ASTER and ground observations

Snow surface temperatures observed by the airborne IR and ASTER imagers were biased warm in comparison with the ground-based snow surface temperature observations at snow pit #2S10. Aircraft flights on two cloud-free days during the study period provided us with 15 overpasses over the ground sites on the western mesa. Two flights were made on 8 February (Figure 7a,b). On the first flight, three overpasses occurred about an hour after sunrise (1413 UTC, 0713 MST) between 1500 and 1630 UTC. The second flight of that day made six overpasses between 1730 and 2000 UTC. The second flight was coincident with the ASTER image taken at about 1808 UTC. On 11 February, a single flight made another six overpasses of the ground site between 1630 and 2000 UTC (Figure 7c,d).

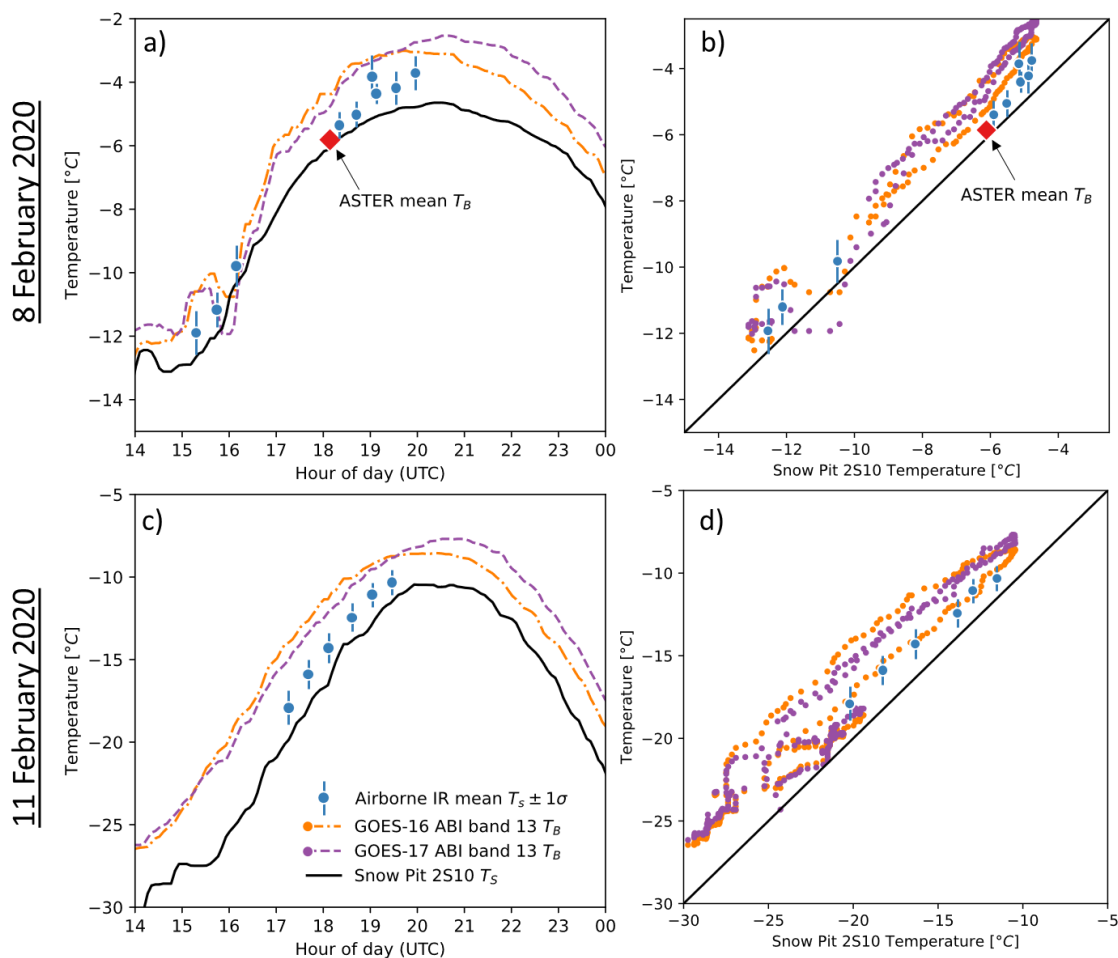


Figure 7. Timeseries for a) 8 Feb. and c) 11 Feb. of the ground-based snow surface temperatures from the Apogee radiometer at snow pit #2S10 (black line), along with GOES-16 (dashed orange) and GOES-17 (dashed purple) band 13 brightness temperatures, airborne IR (blue circles), and ASTER (red diamonds) mean brightness temperatures for the 1 km² area around the ground site. Plots of ground-based snow surface temperature against remote sensing brightness temperatures on b) 8 Feb. and d) 11 Feb.

330

On 8 Feb., snow surface temperatures as seen by the airborne IR and ASTER imagery appeared more uniform than on 11 Feb. around snow pit #2S10, and therefore less sensitive to the size of the area sampled from the imagery to compare with ground-based observations (Table 2). ASTER on 8 February matched most closely to the ground-based surface temperatures with its single pixel value, though this difference only increased by ~ 0.3 °C as the size of the sampled region increased. Snow surface temperatures as seen in the airborne IR imagery were more uniform across the study area on 8 February (with standard deviations across the 1 km² area of 0.2 to 0.6 °C) than on 11 February (with standard deviations of 0.7 to 1.0 °C).

335

Table 2. Mean difference between ground-based snow surface temperatures and surface temperatures from both ASTER and airborne IR imagery, sampled from square areas with sides

Box size of **Mean Difference with Ground-based Ts at Snow Pit 2S10**



image area sampled (m)	ASTER, 8 Feb.	Airborne IR, 8 Feb.	Airborne IR, 11 Feb.
1000	0.3	0.6	2.0
500	0.3	0.9	2.3
250	0.1	0.9	2.0
100	0.0	0.9	1.8
50	-	0.9	1.7
25	-	0.9	1.5
10	-	0.9	1.6
5	-	1.0	1.4

340

Only three snow pits on 8 February, and two snow pits on 11 February were captured in the airborne IR imagery within +/- 30 minutes of their snow surface temperature measurements. On the 8th, two of the snow pit surface temperature measurements were within +/- 1 °C of the airborne IR image, one was ~2 °C warmer, and on the 11 February, both snow pit temperature observations were 3 – 4 °C warmer than the temperatures in the airborne IR images. Measuring the temperature of the top-most centimeter of snow is not trivial, as the stem thermometers used are in contact with snow grains and the air space between snow grains. Near the top of the snowpack, the air temperature can be close to that of the above-surface air (Colbeck, 1989), potentially biasing these snow surface temperature readings more towards that of warmer ambient air temperatures.

345

350

Table 3. Summary of mean differences between the various surface temperature data sources (aggregated across all ABI pixel footprints where applicable) for two days of coincident observations during the SnowEx 2020 field campaign. Cells are colored by sign and magnitude of the difference, with positive differences in red and negative differences in blue.

	Ground Ts	Airborne IR Ts	ASTER Tb	GOES-17 b13 Tb	GOES-17 b14 Tb	GOES-16 b13 Tb	GOES-16 b14 Tb
Ground Ts		0.8	0.3	1.6	1.2	1.3	1
Airborne IR Ts	1.8		0.6	0.3	0	1.1	0.9
ASTER Tb	-	-		2.2	0.6	2.6	1.2
GOES-17 b13 Tb	2.9	1.7	-		-0.3	0.1	0.3
GOES-17 b14 Tb	2.7	1.6	-	-0.2		-0.2	0
GOES-16 b13 Tb	2.7	3.4	-	0.3	0.1		-0.2
GOES-16 b14 Tb	2.4	3.5	-	0.5	0.3	0	

11 February 2020
(difference = row – column)

8 February 2020
(difference = column – row)



4.3 Comparison of high temporal resolution GOES-R ABI with continuous ground observations

Both GOES-16 and -17 reported surface brightness temperatures warmer than the ground-based snow surface temperature observations (Figure 7), though this difference varied over the course of each day (Figure 8). Compared to the ground-based observations, the band 14 brightness temperatures had smaller mean and root-mean-squared differences than did the band 13 brightness temperatures. ABI brightness temperatures and ground-based temperature observations show a hysteresis patterns, with GOES ABI brightness temperatures more closely matching the ground-based observations in the nighttime (11 Feb.) and early morning (8 Feb.) than during the day. This pattern is more apparent on 11 Feb., with GOES brightness temperatures warming up in the morning, and cooling down in the evening, faster than the ground-based snow surface temperatures.

GOES-16 and -17, bands 13 and 14, all observed daily T_{\min} and T_{\max} within 1 hour or less of those measured on the ground, and the DTR matched within ± 3 °C on both days. On 8 February, GOES-16 and -17, bands 13 and 14, all observed T_{\max} within 30 minutes of ground-based T_{\max} . Both GOES-16 and -17 observed a DTR ~ 3 °C larger in this time period than the DTR measured on the ground. On 11 February, GOES-16 bands 13 and 14 observed the time of T_{\max} 30 minutes later than the ground-based T_{\max} , and T_{\min} within 15 minutes. GOES-17 saw T_{\max} almost 1 hour later than ground-based T_{\max} , and a T_{\min} within 20 minutes of ground-based T_{\min} . On this day, the DTR observed by GOES ABI was ~ 3 °C smaller than the DTR from the ground-based snow surface temperature observations.

4.4 Comparison of GOES-R ABI, airborne IR, and ASTER imagery

The surface brightness temperatures from both GOES-16 and -17 were warmer than those from airborne IR and ASTER imagery, and this warm bias was larger for GOES-16, especially for ABI pixels which contained larger forest fractions. The mean differences between GOES-16 and -17 and airborne IR observations across all pixels during the first flight on 8 February decreased over time from a positive to a negative biases (Figure 8a,b). During the second flight, the mean differences between GOES-16 and airborne IR generally decreased from about 2 °C to 0 °C, while the mean differences between GOES-17 and airborne IR increased over time from -1 °C to 1 °C. On 11 February, the mean differences between GOES-17 and airborne IR were relatively constant throughout the morning of observations, while GOES-16 mean differences decreased similarly to what was seen on 8 February, from 5 °C to 2 °C (Figure 8c,d). The mean differences between GOES-16 and airborne IR were found to be larger for ABI pixel footprints with higher f_{veg} , while the differences with GOES-17 did not correlate with f_{veg} (Figure 9). Similarly, the mean differences between GOES-16, but not GOES-17, and ASTER were larger for ABI pixel footprints with larger f_{veg} .

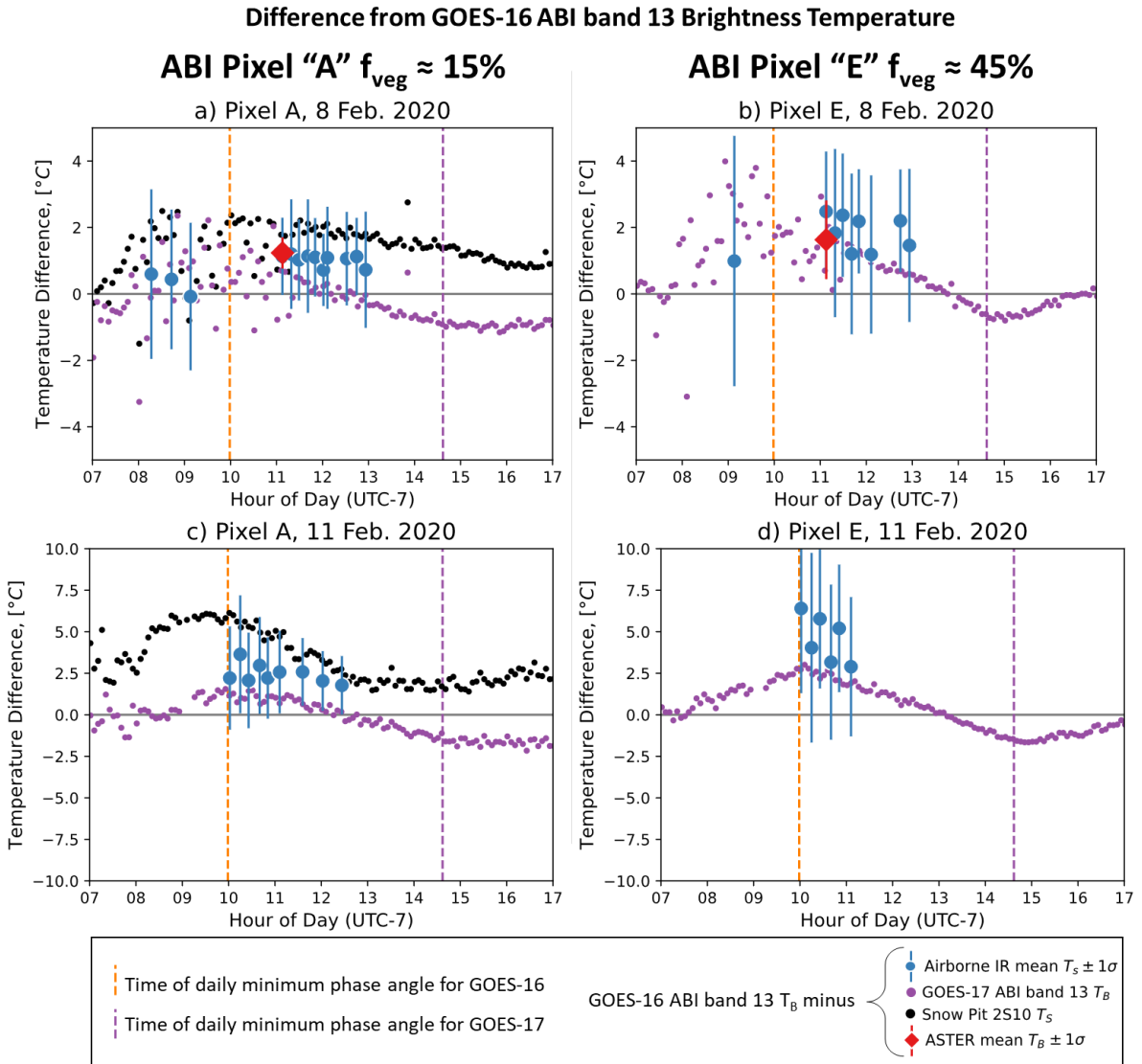


Figure 8. Difference between GOES-16 ABI band 13 brightness temperature, and surface temperature observations from GOES-17 ABI band 13, airborne IR imagery, ASTER imagery, and ground-based observations. Plots for (a,b) 8 February 2020 and (c,d) 11 February 2020 for pixels (a,c) A ($f_{veg} \approx 15\%$) and (b,d) E ($f_{veg} \approx 45\%$). The times that GOES-16 and GOES-17 have their daily minimum phase angle are marked with vertical dashed orange and purple lines, respectively.

The difference between GOES-16 and -17 brightness temperatures showed a prominent pattern over the course of each day, with GOES-16 reporting warmer brightness temperatures by as much as 3 °C in the morning, peaking at about 1700 UTC, and GOES-17 reporting warmer brightness temperatures by nearly 3 °C in the afternoons, peaking at about 2200 UTC. The maximum and minimum differences between GOES-16 and -17 were larger for the more forested pixel E than the mostly open snow pixel A. However, there was no correlation found between these differences and the f_{veg} value of each pixel.

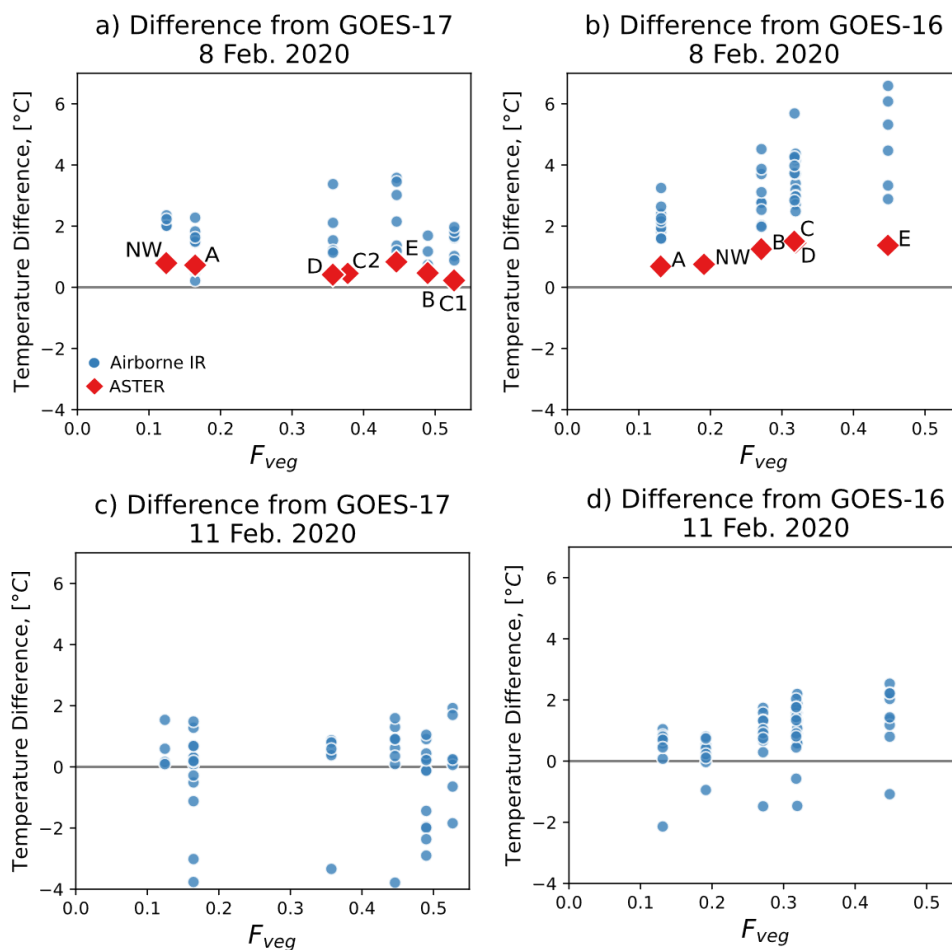


Figure 9. Mean differences between GOES-16 and -17 ABI brightness temperatures, airborne IR (blue dots) and ASTER (red diamonds), plotted against the fractional vegetated area (f_{veg}) value of each ABI pixel footprint.

5 Discussion

395 5.1 Intercomparison of remote sensing data

The mean differences between surface temperatures observed by all remote sensing sources and ground-based observations ranged from about 0 to 5 °C, with remote sensing sources (airborne IR, ASTER, GOES ABI) typically reporting warmer surface temperatures than those measured on the ground. The airborne IR and ASTER images best matched the ground-based snow surface temperature observations because they could resolve separate snow and forest temperatures, whereas the
 400 coarser 2+ km spatial resolution GOES-R ABI pixels reported a mixture of forest and snow temperatures (Table 3). This was apparent even for the mostly forest-free westernmost portion of Grand Mesa (pixels A) with $f_{veg} \approx 15\%$. Additionally, there were some thin high-altitude clouds on the morning of 8 February, visible in the GOES-R ABI near-infrared “cirrus band”

(band 4, 1.37 μm). The timeseries of band 13 and 14 brightness temperatures during this time show rapid changes, and possibly colder temperatures than would be reported if those thin clouds had not been present.

405 Over the course of each morning, the airborne IR imagery tracked the morning warm-up of the snow surface closely, with a constant warm bias relative to the ground-based observations (Figure 7). GOES-16 and -17 ABI also tracked the ground-based snow surface temperature observations over the course of the day, though their biases relative to those observations changed over time (Figure 8). Snow surface temperatures were more uniform across the western mesa on 8 February than on 11 February, as seen in airborne imagery (Table 2). This was also reflected in ABI brightness temperatures more closely
410 matching the ground-based observations on 8 February. Both GOES-16 and -17 captured the timing of daily T_{\min} and T_{\max} on these two days within ~ 1 hour, and the diurnal temperature range within ± 3 $^{\circ}\text{C}$. This uncertainty in the DTR is similar to the range seen in the mean differences over each day and across the mesa between GOES-R ABI and the ground-based observations (1-3 $^{\circ}\text{C}$), ABI and ASTER (2 – 3 $^{\circ}\text{C}$), and ABI and the airborne IR imagery (0 – 5 $^{\circ}\text{C}$).

Our use of a ground-based infrared radiometer, and thermal infrared imagers all within the 8-14 μm window allowed us to
415 directly compare their observed brightness temperatures rather than derived LST products. The thermal infrared brightness temperatures observed by ABI are likely to be colder than the actual surface brightness temperature due to atmospheric absorption of infrared radiation. At our high elevation study site, the atmospheric path is shorter, and atmospheric water vapor concentrations are less than those at lower elevations. However, we could still expect brightness temperatures to appear nearly 4 $^{\circ}\text{C}$ colder than true surface brightness temperatures for these GOES-R ABI observations (Berk et al., 2014).
420 The GOES-R ABI LST product, which is designed to account for these atmospheric effects, reported surface temperatures about 3-4 $^{\circ}\text{C}$ warmer than the ground-based observations of brightness temperatures. Absorption by water vapor along the atmospheric path between the snow surface and the radiometer mounted < 2 m above the snow surface is negligible; however, for the airborne IR observations with a path length of ~ 1 km, this could result in brightness temperatures nearly 2 $^{\circ}\text{C}$ colder than true surface brightness temperatures. Due to the difference in atmospheric path length alone we would expect
425 satellite observations of top of atmosphere brightness temperature to be biased colder than airborne observations from ~ 1 km. However, our results instead show GOES-R ABI brightness temperatures biased warmer than airborne observations, suggesting that the magnitude of the atmospheric effect is surpassed by view angle related effects.

The mean differences between ground-based snow surface temperature observations and ABI band 14 brightness temperatures were smaller than those for band 13 by about 0.2-0.4 $^{\circ}\text{C}$. This, however, doesn't necessarily mean that band 14
430 was providing a more accurate snow surface temperature reading. Band 14 covers wavelengths where we can expect some absorption of infrared radiance by atmospheric water vapor, whereas band 13 sits within the "clean IR" window with minimal to no IR absorption by water vapor (Schmit et al., 2018). With no atmospheric water vapor absorption, the difference between band 13 and 14 brightness temperatures would be negligible. Any atmospheric water vapor present can result in band 14 brightness temperatures being colder than band 13, as was the case seen here. Though we chose cloud-free
435 time periods of observations, any trace amounts of water vapor could be causing band 14 to appear colder, and which coincidentally more closely matched snow surface temperatures on Grand Mesa.



5.2 Sun-satellite phase angle and thermal infrared shadow-hiding

Even with the flat terrain of Grand Mesa controlling for effects of viewing mountain terrain from off-nadir angles (Pestana and Lundquist, 2022), we observed a morning warm bias between GOES-16 and the coincident nadir-looking ASTER, 440 airborne IR imagery, and GOES-17 (Figure 8). The GOES-16 brightness temperatures were potentially exhibiting a hotspot effect when the angle between the sun and the view angle of GOES-16 (phase angle) reached a daily minimum. The hotspot effect seen in remote sensing imagery of forests is understood to be explained by shadow-hiding in imagery of reflected sunlight in the visible and NIR wavelengths (Deering et al., 1999; Hapke et al., 1996).

When the airborne IR and ASTER images were taken (1400-2000 UTC), the sun was rising in the southeastern sky, in the 445 same direction from which GOES-16 was viewing Grand Mesa. At about 1700 UTC on 11 February, when we see the largest warm biases between GOES-16 and all other datasets, the sun had reached 26.9 degrees elevation at an azimuth of 139.1 degrees (26.1 and 139.6 on the 8th). The angle between GOES-16's view and the sun's position (phase angle) was at its minimum of ~ 8 degrees on 11 February at 1659 UTC (~9 degrees at the same time on 8 February). At this time, the sun was illuminating and warming the southeastern facing sides of trees that GOES-16 is viewing, which in the airborne IR 450 imagery were as much as 5 °C warmer than the shaded side of trees (Figure 2). In addition to viewing the sunlit side of trees, snow in tree shadows was considerably colder than snow in the sunlight (by ~10 °C) and would also be hidden from the view of GOES-16.

The airborne IR and ASTER images viewed the study area from nadir, and the difference between these two image sources did not vary with f_{veg} . GOES-17 surface brightness temperatures had smaller mean differences compared to airborne and 455 ASTER than GOES-16, and these differences did not correlate with f_{veg} . GOES-17, viewing Grand Mesa from the southwest, would similarly be viewing the southwest facing sides of trees, though during the morning these would be partially in sun and partially in shade. In the afternoon we see that GOES-17 is warmer than GOES-16, peaking at about 2200 UTC. The minimum phase angle between the sun and GOES 17 is ~8 degrees at 2137 UTC on 11 February (~9 degrees on 8 Feb.).

Though we see that the warm bias in GOES-16 imagery correlates with f_{veg} , the presence of these same warm biases and 460 their patterns over time (e.g. warm biases peaking at the time of minimum phase angle) in the mostly open snow pixels (Figure 8, A) suggests that other sources of surface roughness may also be contributing to this effect, such as greater than meter-scale dunes, or sub-meter-scale ripples and sastrugi (Kochanski et al., 2019; Warren et al., 1998).

5.3 Applications for downscaling GOES-R ABI thermal infrared imagery

Downscaling methods for coarse spatial resolution thermal infrared imagery rely on finer spatial resolution maps of land 465 cover properties and statistical relationships to model and therefore correct for the expected biases in the coarse imagery. Prior methods have used vegetation (Inamdar and French, 2009; Kustas et al., 2003) and terrain maps (Walters, 2013), and biases in GOES-16 ABI imagery have been related to their off-nadir views of complex terrain (Pestana and Lundquist, 2022). Our results demonstrate that for high temporal resolution GOES-R ABI thermal infrared imagery, not only does the



fractional forest coverage of each ABI pixel have some control on surface temperature biases, but so does the solar
470 illumination angle, and the phase angle between the satellite and sun. Thus, any downscaling of GOES-R data must
explicitly consider time of day and time of year. These solar and satellite view angle controls on surface temperature
observation biases were observed at both the forested and open snow regions of Grand Mesa, suggesting that surface
roughness features as large as trees but perhaps as small as sastrugi contributed to the hotspot effect seen. This information
will be needed to determine if, when, and what magnitude a hotspot or thermal infrared shadow-hiding effect will have on
475 the surface temperature bias of the coarser resolution GOES-R ABI.

6 Conclusions

During the NASA SnowEx field campaign in February 2020, we conducted an intercomparison of thermal infrared remote
sensors for retrieving surface brightness temperatures of snow and forests. The flat study site at Grand Mesa in western
Colorado, USA, allowed us to investigate the impact that forest cover has on thermal infrared remote sensing from GOES-16
480 and GOES-17 at off-nadir view angles and high temporal resolution. Snow surface temperatures observed by the airborne IR
and ASTER imagers were biased warm in comparison with the ground-based snow surface temperature observations, and
the airborne IR imagery itself was found to have a warm bias compared with ASTER, all with mean differences within < 1
 $^{\circ}\text{C}$ of each other. GOES-16 and GOES-17 observed daily maximum and minimum brightness temperatures within ~ 1 hour of
those measured in situ, and the diurnal temperature range within ± 3 $^{\circ}\text{C}$. GOES-16 and GOES-17 reported warmer surface
485 brightness temperatures than the ground-based, airborne IR, and ASTER observations. This warm bias was larger for GOES-
16 in the mornings when the aircraft and ASTER passed over the study site. The maximum warm biases in GOES-16 and
GOES-17 occurred when the sun-satellite phase angle was at its daily minimum, suggesting that a thermal infrared shadow-
hiding effect may cause these off-nadir imagers to sense warmer temperatures than nadir-looking imagers.

The thermal infrared imagery and ground-based snow surface temperature observations collected as part of SnowEx 2020
490 provide a unique dataset for characterizing the high temporal resolution observations from geostationary satellites. It could
be used further for testing methods for spatially downscaling coarse GOES-R ABI imagery of snow and forests to finer
spatial resolutions with statistical models, sensor fusion methods (Quan et al., 2018; Weng and Fu, 2014), or using spectral
mixture models to separate snow and forest temperatures (Lundquist et al., 2018). Though this work focuses on a single site
in a short time period, other geostationary satellites comparable to GOES-R ABI, such as Fengyun-4 and Himawari-8,
495 provide similar views of High Mountain Asia and other mountains in the Eastern hemisphere where these observations are
needed. We expect the processes described here to be important for interpreting geostationary thermal IR observations all
around the globe.



7 Code availability

The code used in the analysis of these datasets, including python scripts and Jupyter Notebooks to generate plots and figures,
500 are available at <https://github.com/spetana/snowex2020/tree/v1.0> (Pestana, 2023)

8 Data availability

All data used in this work is publicly accessible. The continuous snow surface temperature observations (Pestana and
Lundquist, 2021), instantaneous snow surface temperatures (Vuyovich et al., 2021; Johnson et al., 2023), and airborne IR
505 imagery (Chickadel et al., 2022) are available through the National Snow and Ice Data Center (NSIDC). The ASTER
imagery is accessible through the USGS LPDAAC (<https://lpdaac.usgs.gov/>), and NOAA Geostationary Operational
Environmental Satellites (GOES) 16 & 17 imagery from <https://registry.opendata.aws/noaa-goes/> with goespy (Mello and
Pestana, 2022).

9 Competing interests

The contact author has declared that none of the authors has any competing interests.

510 10 Acknowledgements

We would like to thank the SnowEx 2020 organizing team, participants, snowmobile guides, National Snow and Ice Data
Center staff, and the Naval Postgraduate School pilots for facilitating the data collection, and the SWESARR team for
accommodating our work and providing IMU/GPS navigation data. We would also like to thank fellow project team
members from SnowEx Hackweek 2021 for their work developing workflows and tools to analyze the SnowEx snow
515 temperature observations: Aji John, Jeremy Johnston, Friedrich Knuth, Jewell Lund, Giulia Mazzotti, Zachary Miller,
Wenge Ni-Meister, Dillon Ragar. Thank you to the University of Washington Mountain Hydrology group for feedback and
input throughout this project. This work was funded by NASA FINESST grant 80NSSC20K1610 and NASA grant
80NSSC20K0374.

References

520 Abrams, M.: The Advanced Spaceborne Thermal Emission and Reflection Radiometer (ASTER): Data products for the high
spatial resolution imager on NASA's Terra platform, *Int. J. Remote Sens.*, 21, 847–859,
<https://doi.org/10.1080/014311600210326>, 2000.



- 525 Balick, L. K., Jerrell R., B., Smith, J. A., and Goltz, S. M.: Directional satellite thermal IR measurements and modeling of a forest in winter and their relationship to air temperature, in: Remote Sensing for Agriculture, Ecosystems, and Hydrology III, Remote Sensing for Agriculture, Ecosystems, and Hydrology III, 162–169, <https://doi.org/10.1117/12.454212>, 2002.
- Berk, A., Conforti, P., Kennett, R., Perkins, T., Hawes, F., and van den Bosch, J.: MODTRAN6: a major upgrade of the MODTRAN radiative transfer code, in: Algorithms and Technologies for Multispectral, Hyperspectral, and Ultraspectral Imagery XX, vol. 9088, edited by: Miguel Velez-Reyes and Fred A. Kruse, Proceedings of SPIE, 90880H-90880H-7, 2014.
- 530 Bréon, F.-M., Maignan, F., Leroy, M., and Grant, I.: Analysis of hot spot directional signatures measured from space, *J. Geophys. Res. Atmospheres*, 107, AAC 1-1-AAC 1-15, <https://doi.org/10.1029/2001JD001094>, 2002.
- Chickadel, C. Chris, Pestana, S. J., and Lundquist, J. D.: SnowEx20 APL-UW CASIE Airborne TIR Mosaic Imagery, Version 1., 2022.
- Colbeck, S. C.: Air Movement in Snow Due to Windpumping, *J. Glaciol.*, 35, 209–213, <https://doi.org/10.3189/S0022143000004524>, 1989.
- 535 Coulston, J. W., Moisen, G. G., Wilson, B. T., Finco, M. V., Cohen, W. B., and Brewer, C. K.: Modeling Percent Tree Canopy Cover: A Pilot Study, *Photogramm. Eng. Remote Sens.*, 78, 715–727, 2012.
- Currier, W. R., Pflug, J., Mazzotti, G., Jonas, T., Deems, J. S., Bormann, K. J., Painter, T. H., Hiemstra, C. A., Gelvin, A., Uhlmann, Z., Spaete, L., Glenn, N. F., and Lundquist, J. D.: Comparing Aerial Lidar Observations With Terrestrial Lidar and Snow-Probe Transects From NASA’s 2017 SnowEx Campaign, *Water Resour. Res.*, 55, 6285–6294, 540 <https://doi.org/10.1029/2018WR024533>, 2019.
- Deering, D. W., Eck, T. F., and Banerjee, B.: Characterization of the Reflectance Anisotropy of Three Boreal Forest Canopies in Spring–Summer, *Remote Sens. Environ.*, 67, 205–229, [https://doi.org/10.1016/S0034-4257\(98\)00087-X](https://doi.org/10.1016/S0034-4257(98)00087-X), 1999.
- Dozier, J.: A method for satellite identification of surface temperature fields of subpixel resolution, *Remote Sens. Environ.*, 11, 221–229, [https://doi.org/10.1016/0034-4257\(81\)90021-3](https://doi.org/10.1016/0034-4257(81)90021-3), 1981.
- 545 Essery, R., Morin, S., Lejeune, Y., and B Ménard, C.: A comparison of 1701 snow models using observations from an alpine site, *Adv. Water Resour.*, 55, 131–148, <https://doi.org/10.1016/j.advwatres.2012.07.013>, 2013.
- Flanner, M. G. and Zender, C. S.: Linking snowpack microphysics and albedo evolution, *J. Geophys. Res. Atmospheres*, 111, 1–12, <https://doi.org/10.1029/2005JD006834>, 2006.
- 550 Hall, D., Box, J., Casey, K., Hook, S., Shuman, C., and Steffen, K.: Comparison of satellite-derived and in-situ observations of ice and snow surface temperatures over Greenland, *Remote Sens. Environ.*, 112, 3739–3749, <https://doi.org/10.1016/j.rse.2008.05.007>, 2008.
- Hall, D. K., Foster, J. L., Irons, J. R., and Dabney, P. W.: Airborne bidirectional radiances of snow-covered surfaces in Montana, U.S.A., *Ann. Glaciol.*, 17, 35–40, <https://doi.org/10.3189/S0260305500012581>, 1993.
- 555 Hapke, B., DiMucci, D., Nelson, R., and Smythe, W.: The cause of the hot spot in vegetation canopies and soils: Shadow-hiding versus coherent backscatter, *Remote Sens. Environ.*, 58, 63–68, [https://doi.org/10.1016/0034-4257\(95\)00257-X](https://doi.org/10.1016/0034-4257(95)00257-X), 1996.



- Henderson, B. G., Balick, L. K., Rodger, A. P., and Pope, P. A.: Concurrent measurements of directional reflectance and temperature of a wintertime coniferous forest from space, *Optical Science and Technology*, SPIE's 48th Annual Meeting, San Diego, California, USA, 21, <https://doi.org/10.1117/12.506296>, 2003.
- 560 Immerzeel, W. W., Lutz, A. F., Andrade, M., Bahl, A., Biemans, H., Bolch, T., Hyde, S., Brumby, S., Davies, B. J., Elmore, A. C., Emmer, A., Feng, M., Fernández, A., Haritashya, U., Kargel, J. S., Koppes, M., Kraaijenbrink, P. D. A., Kulkarni, A. V., Mayewski, P. A., Nepal, S., Pacheco, P., Painter, T. H., Pellicciotti, F., Rajaram, H., Rupper, S., Sinisalo, A., Shrestha, A. B., Viviroli, D., Wada, Y., Xiao, C., Yao, T., and Baillie, J. E. M.: Importance and vulnerability of the world's water towers, *Nature*, 577, 364–369, <https://doi.org/10.1038/s41586-019-1822-y>, 2020.
- 565 Inamdar, A. K. and French, A.: Disaggregation of GOES land surface temperatures using surface emissivity: DISAGGREGATION OF GOES LST, *Geophys. Res. Lett.*, 36, n/a-n/a, <https://doi.org/10.1029/2008GL036544>, 2009.
- Johnson, M., Sandusky, M., and Marshall, H.: SnowEx/snowexsql: SnowEx Hackweek 2022 release | Zenodo, 2023.
- Kim, Y., Still, C. J., Roberts, D. A., and Goulden, M. L.: Thermal infrared imaging of conifer leaf temperatures: Comparison to thermocouple measurements and assessment of environmental influences, *Agric. For. Meteorol.*, 248, 361–371, 570 <https://doi.org/10.1016/j.agrformet.2017.10.010>, 2018.
- Kochanski, K., Anderson, R. S., and Tucker, G. E.: The evolution of snow bedforms in the Colorado Front Range and the processes that shape them, *The Cryosphere*, 13, 1267–1281, <https://doi.org/10.5194/tc-13-1267-2019>, 2019.
- Kustas, W. P., Norman, J. M., Anderson, M. C., and French, A. N.: Estimating subpixel surface temperatures and energy fluxes from the vegetation index–radiometric temperature relationship, *Remote Sens. Environ.*, 85, 429–440, 575 [https://doi.org/10.1016/S0034-4257\(03\)00036-1](https://doi.org/10.1016/S0034-4257(03)00036-1), 2003.
- Lapo, K. E., Hinkelman, L. M., Raleigh, M. S., and Lundquist, J. D.: Impact of errors in the downwelling irradiances on simulations of snow water equivalent, snow surface temperature, and the snow energy balance, *Water Resour. Res.*, 51, 1649–1670, <https://doi.org/10.1002/2014WR016259>, 2015.
- 580 Lundquist, J. D., Chickadel, C., Cristea, N., Currier, W. R., Henn, B., Keenan, E., and Dozier, J.: Separating snow and forest temperatures with thermal infrared remote sensing, *Remote Sens. Environ.*, 209, 764–779, <https://doi.org/10.1016/j.rse.2018.03.001>, 2018.
- Mello, P. A. and Pestana, S.: *spetana/goes-py: v0.2.2*, <https://doi.org/10.5281/zenodo.6455060>, 2022.
- 585 Meyer, D., Siemonsma, D., Brooks, B., and Johnson, L.: Advanced Spaceborne Thermal Emission and Reflection Radiometer Level 1 Precision Terrain Corrected Registered At-Sensor Radiance (AST_L1T) Product, algorithm theoretical basis document, Advanced Spaceborne Thermal Emission and Reflection Radiometer Level 1 Precision Terrain Corrected Registered At-Sensor Radiance (AST_L1T) Product, algorithm theoretical basis document, U.S. Geological Survey, Reston, VA, <https://doi.org/10.3133/ofr20151171>, 2015.
- 590 Niu, G.-Y., Yang, Z.-L., Mitchell, K. E., Chen, F., Ek, M. B., Barlage, M., Kumar, A., Manning, K., Niyogi, D., Rosero, E., Tewari, M., and Xia, Y.: The community Noah land surface model with multiparameterization options (Noah-MP): 1. Model description and evaluation with local-scale measurements, *J. Geophys. Res.*, 116, D12109, <https://doi.org/10.1029/2010JD015139>, 2011.
- Pestana, S.: *spetana/snowex2020: Initial release*, <https://doi.org/10.5281/zenodo.8209719>, 2023.



- Pestana, S. and Lundquist, J. D.: SnowEx20 Raw Near Surface Snow Temperature Profile Time Series, Version 1, , <https://doi.org/10.5067/9HYQMFZP4ALB>, 2021.
- 595 Pestana, S. and Lundquist, J. D.: Evaluating GOES-16 ABI surface brightness temperature observation biases over the central Sierra Nevada of California, *Remote Sens. Environ.*, 281, 113221, <https://doi.org/10.1016/j.rse.2022.113221>, 2022.
- Pestana, S., Chickadel, C. C., Harpold, A., Kostadinov, T. S., Pai, H., Tyler, S., Webster, C., and Lundquist, J. D.: Bias Correction of Airborne Thermal Infrared Observations Over Forests Using Melting Snow, *Water Resour. Res.*, 55, 11331–11343, <https://doi.org/10.1029/2019WR025699>, 2019.
- 600 Pestana, S., Bhushan, S., and Carter, J.: `spestana/goes-ortho`: Initial release | Zenodo, 2022.
- Quan, J., Zhan, W., Ma, T., Du, Y., Guo, Z., and Qin, B.: An integrated model for generating hourly Landsat-like land surface temperatures over heterogeneous landscapes, *Remote Sens. Environ.*, 206, 403–423, <https://doi.org/10.1016/j.rse.2017.12.003>, 2018.
- 605 Raleigh, M. S., Landry, C. C., Hayashi, M., Quinton, W. L., and Lundquist, J. D.: Approximating snow surface temperature from standard temperature and humidity data: New possibilities for snow model and remote sensing evaluation: Snow Surface Temperature Approximation, *Water Resour. Res.*, 49, 8053–8069, <https://doi.org/10.1002/2013WR013958>, 2013.
- Raleigh, M. S., Livneh, B., Lapo, K., and Lundquist, J. D.: How Does Availability of Meteorological Forcing Data Impact Physically Based Snowpack Simulations?*, *J. Hydrometeorol.*, 17, 99–120, <https://doi.org/10.1175/JHM-D-14-0235.1>, 2016.
- 610 Rittger, K., Raleigh, M. S., Dozier, J., Hill, A. F., Lutz, J. A., and Painter, T. H.: Canopy Adjustment and Improved Cloud Detection for Remotely Sensed Snow Cover Mapping, 0–2 pp., <https://doi.org/10.1029/2019wr024914>, 2019.
- Schmit, T. J., Griffith, P., Gunshor, M. M., Daniels, J. M., Goodman, S. J., and Lehair, W. J.: A Closer Look at the ABI on the GOES-R Series, *Bull. Am. Meteorol. Soc.*, 98, 681–698, <https://doi.org/10.1175/BAMS-D-15-00230.1>, 2017.
- Schmit, T. J., Lindstrom, S. S., Gerth, J. J., and Gunshor, M. M.: Applications of the 16 spectral bands on the Advanced Baseline Imager (ABI), *J. Oper. Meteorol.*, 06, 33–46, <https://doi.org/10.15191/nwajom.2018.0604>, 2018.
- 615 Selkowitz, D., Forster, R., and Caldwell, M.: Prevalence of Pure Versus Mixed Snow Cover Pixels across Spatial Resolutions in Alpine Environments, *Remote Sens.*, 6, 12478–12508, <https://doi.org/10.3390/rs61212478>, 2014.
- Shamir, E. and Georgakakos, K. P.: MODIS Land Surface Temperature as an index of surface air temperature for operational snowpack estimation, *Remote Sens. Environ.*, 152, 83–98, <https://doi.org/10.1016/j.rse.2014.06.001>, 2014.
- 620 Stillinger, T., Roberts, D. A., Collar, N. M., and Dozier, J.: Cloud Masking for Landsat 8 and MODIS Terra Over Snow-Covered Terrain: Error Analysis and Spectral Similarity Between Snow and Cloud, *Water Resour. Res.*, 55, 6169–6184, <https://doi.org/10.1029/2019WR024932>, 2019.
- Tomasi, E., Giovannini, L., Zardi, D., and de Franceschi, M.: Optimization of Noah and Noah_MP WRF Land Surface Schemes in Snow-Melting Conditions over Complex Terrain, *Mon. Weather Rev.*, 145, 4727–4745, <https://doi.org/10.1175/MWR-D-16-0408.1>, 2017.
- 625 US Geologic Survey: 1 Arc-second Digital Elevation Models (DEMs)—USGS National Map 3DEP Downloadable Data Collection., 2017.



- Vuyovich, C. M., Marshall, H., Elder, K., Hiemstra, C., Brucker, L., and McCormick, M.: SnowEx20 Grand Mesa Intensive Observation Period Snow Pit Measurements, Version 1, , <https://doi.org/10.5067/DUD2VZEVBJS>, 2021.
- 630 Walters, R. D.: Transfer of Snow Information across the Macro-to-Hillslope-Scale Gap Using a Physiographic Downscaling Approach: Implications for Hydrologic Modeling in Semiarid, Seasonally Snow-Dominated Watersheds, 2013.
- Wan, Z., Zhang, Y., Zhang, Q., and Li, Z.: Validation of the land-surface temperature products retrieved from Terra Moderate Resolution Imaging Spectroradiometer data, *Remote Sens. Environ.*, 83, 163–180, [https://doi.org/10.1016/S0034-4257\(02\)00093-7](https://doi.org/10.1016/S0034-4257(02)00093-7), 2002.
- Warren, S. G.: Optical properties of snow, *Rev. Geophys.*, 20, 67–89, <https://doi.org/10.1029/RG020i001p00067>, 1982.
- 635 Warren, S. G.: Optical properties of ice and snow, *Philos. Trans. R. Soc. Math. Phys. Eng. Sci.*, 377, 20180161, <https://doi.org/10.1098/rsta.2018.0161>, 2019.
- Warren, S. G., Brandt, R. E., and O’Rawe Hinton, P.: Effect of surface roughness on bidirectional reflectance of Antarctic snow, *J. Geophys. Res. Planets*, 103, 25789–25807, <https://doi.org/10.1029/98JE01898>, 1998.
- 640 Weng, Q. and Fu, P.: Modeling diurnal land temperature cycles over Los Angeles using downscaled GOES imagery, *ISPRS J. Photogramm. Remote Sens.*, 97, 78–88, <https://doi.org/10.1016/j.isprsjprs.2014.08.009>, 2014.